Deep Ultraviolet Plasmon Resonance in Aluminum Nanoparticle Arrays

Giulia Maidecchi,[†,▲] Grazia Gonella,[‡,▲,*] Remo Proietti Zaccaria,[§] Riccardo Moroni,[⊥] Luca Anghinolfi,[†,△] Angelo Giglia,[∥] Stefano Nannarone,[∥,¶] Lorenzo Mattera,[†] Hai-Lung Dai,[‡] Maurizio Canepa,[†] and Francesco Bisio[⊥,*]

[†]CNISM, Sede Consorziata di Genova and Dipartimento di Fisica, Università di Genova, Via Dodecaneso 33, I-16146 Genova, Italy, [‡]Department of Chemistry, Temple University, Philadelphia, Pennsylvania 19122, United States, [§]Istituto Italiano di Tecnologia, Via Morego 30, 16163 Genova, Italy, [⊥]CNR-SPIN, C.so Perrone 24, I-16152 Genova, Italy, [∥]CNR-Istituto Officina Materiali, I-34149 Trieste, Italy, and [¶]Dipartimento di Ingegneria E. Ferrari, Università di Modena e Reggio Emilia, I-41125, Modena, Italy. [▲]These authors contributed equally to this work. [△]Present address: Laboratory for Micro- and Nanotechnology, Paul Scherrer Institut, 5232 Villigen PSI, Switzerland.

ABSTRACT Small aluminum nanoparticles have the potential to exhibit localized surface plasmon resonances in the deep ultraviolet region of the electromagnetic spectrum, however technical and scientific challenges make it difficult to attain this limit. We report the fabrication of arrays of Al/Al_2O_3 core/shell nanoparticles with a metallic-core diameter between 12 and 25 nm that display sharp plasmonic resonances at very high energies, up to 5.8 eV (down to $\lambda = 215$ nm). The arrays were fabricated by means of a straightforward self-organization approach. The experimental spectra were compared with theoretical calculations that allow the correlation of each feature to the corresponding plasmon modes.

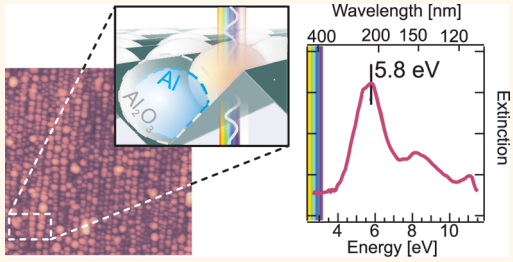

KEYWORDS: aluminum · ultraviolet · nanoparticle · discrete-dipole approximation · finite integration technique · self-organization

The localized surface plasmon (LSP) is a collective oscillation of the free-electron gas within metallic nanostructures excited by an external electromagnetic (EM) field.[1−6] Sharp LSP resonances (LSPRs) require small dielectric losses in the metal. Thus, although the LSPR is a very general feature of metals,[7−10] most of the research in plasmonics has, so far, focused on a handful of materials, typically Au or Ag. Beyond these noble metals, however, other, less exploited metals exist, whose specific characteristics could significantly broaden the current reach of plasmonics, possibly through the integration of new functionalities (magnetic, catalytic, chemical).[9−15]

Among these "novel" plasmonic materials, there is a surging interest in aluminum in fundamental studies,[9,11,12,16−25] plasmon-enhanced photovoltaics,[26−28] and nonlinear optical spectroscopies.[17,29−31] The dielectric response of Al[32,33] yields an LSPR that, for small particles, is well within the deep ultraviolet (DUV) optical range,[20,34,35] and whose sharpness and intensity improve with increasing energy. In addition, the Al LSPRs are much more sensitive than those of most other materials to the nanoparticle (NP) geometrical characteristics,[9,11,16,25] allowing one to tune the LSPR energy from the DUV to the IR by a relatively small change of the particle size. The excellent field enhancement performances of Al make it an excellent material for nanoantennas and nonlinear optical spectroscopies (*e.g.*, Raman).[17,19,22,23,25,29−31,36,37] Last but not least, Al is significantly more abundant, hence cheaper, than most other metals, a particularly appealing factor for sustainable photovoltaics.

Despite its potential, the exploitation of Al in plasmonics is very recent and still facing both scientific and technical challenges. From the fabrication point of view, the strong size dependence of the LSPR may turn to a potential disadvantage when, in the absence of narrow particle size distributions, sharp LSPRs quickly turn into broad, featureless spectra.[38] Compared to its Au and Ag noble metal counterparts, Al is significantly more difficult to synthesize in the few nanometer size regime[39,40] and quickly oxidizes upon exposure to atmosphere,[41] turning the outer metallic layer into oxide

* Address correspondence to francesco.bisio@spin.cnr.it, gonella@temple.edu.

Received for review February 22, 2013 and accepted June 2, 2013.

Published online June 02, 2013
10.1021/nn400918n

and red shifting the LSPR.[16,18,20] While oxidation represents a relatively minor issue for larger Al particles (several tens of nanometers), its impact is huge on the smaller NPs, the most interesting for DUV applications. Therefore, the small-particle limit of the Al LSPR, most important for ushering plasmonics into the DUV spectral regions, has so far remained largely unexplored.

In this work, we report on the DUV plasmonic response of Al/Al_2O_3 core/shell NPs with metallic-core diameter in the 12−25 nm range. The NPs are fabricated by a self-organization approach, arranged in two-dimensional ordered arrays supported on spontaneously nanopatterned LiF single crystals. The core−shell NPs exhibit sharp DUV LSPRs at photon energies ranging from 4.2 eV ($\lambda = 295$ nm) to 5.8 eV ($\lambda = 215$ nm), depending on size and excitation geometry, among the highest LSPR energies ever observed in NPs by optical spectroscopy. The comparison of the experimental data with discrete dipole approximation (DDA) and finite integration technique (FIT) calculations allows us to clearly ascribe each feature present in the optical response of the system to the corresponding plasmon modes.

RESULTS AND DISCUSSION

The Al NPs were fabricated starting from wedge-shaped Al films grown onto a single nanopatterned LiF substrate. The NPs obtained for an Al/LiF equivalent coverage of 1.7, 2.5, and 3.4 nm, henceforth referred to as "zone" 1, 2, and 3 ($z1$, $z2$, $z3$), respectively, will be addressed in this work. Details of sample preparation are reported in Materials and Methods. A general scheme of the NP fabrication is shown in Figure 1, top panel. The size and shape of the NPs, their chemical composition, and their arrangement in the 2D array are all fundamental ingredients that determine their optical response. These parameters were deduced by means of a combined atomic force microscopy (AFM) and high-resolution X-ray photoelectron spectroscopy (HR-XPS) study and subsequently used in calculations.

Morphology and Chemical Composition. In Figure 1A−C, three representative AFM images of $z1$, $z2$, and $z3$ are reported. In the images, we clearly distinguish small, seemingly spheroidal, agglomerates aligned along the LiF nanoridges, whose mean size gradually increased with increasing coverage. The substrate morphology acts as an effective barrier to atom mobility, favoring the formation of NP arrangement with a size distribution narrower than that obtained with unconstrained Al dewetting.[38] The NPs in the images were digitally isolated with carefully applied threshold algorithms, yielding so-called "masks", shown superimposed on the left-hand sides of Figure 1A−C, in which each NP is represented by a white area against a black background. The area and aspect ratio of such white regions are not a reliable measure of the actual NP size and shape, yet masks provide a robust estimate of the NP

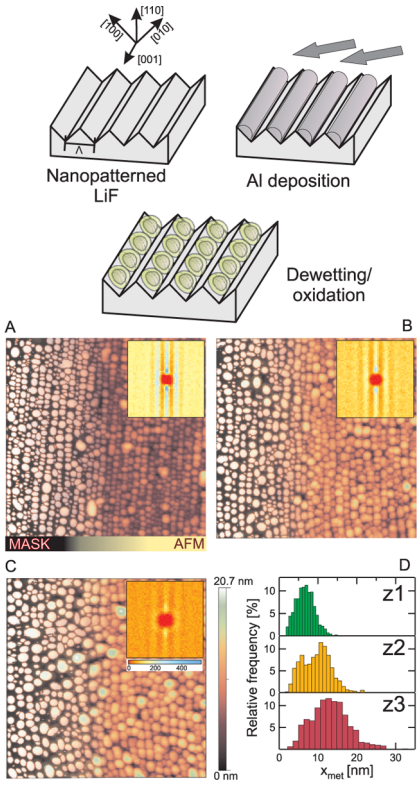

Figure 1. Top: Schematic representation of the Al NP array fabrication procedure. (A−C) AFM images of the Al/LiF systems obtained for an Al coverage of 1.7 nm (A, $z1$), 2.5 nm (B, $z2$), and 3.4 nm (C, $z3$). The left-hand side of each AFM image reports the masks obtained by means of image thresholding algorithms with the aim of isolating the NPs. The AFM image size is 800 × 800 nm^2. The z-axis color scale is the same for all images. Insets of panels A−C: 2D interparticle distance autocorrelation extracted from the masks. The inset size is 200 × 200 nm^2 for all insets. (D) Histograms of the NP semiaxis length as a function of Al coverage. The mean semiaxis length was deduced by XPS analysis (shown later in this work).

density in the arrays, their spatial correlation, and their relative size distribution.

The NP density ρ deduced by AFM is determined to be $\rho = 1750 \pm 40$, 1300 ± 30, and 950 ± 30 NP/μm^2 for $z1$, $z2$, and $z3$, respectively. Knowledge of the corresponding equivalent coverage, hence of the number of Al atoms deposited per unit area, allowed us to deduce from ρ the mean number N_{Al} of Al atoms per particle (metal and oxide), which is $N_{Al} = 6 \times 10^4$, 1.2×10^5, and 2.2×10^5 for $z1$−$z3$. In Figure 1D, we report the histograms of the NP semiaxis, deduced from the digitized AFM images. The distributions have been "normalized" to the mean NP semiaxis deduced by XPS analysis (discussed later in this work). The size distributions are in all cases relatively broad and show a slight tendency to become bimodal for increasing coverage, due to small NPs clustering around larger particles. The autocorrelation of the NP center-to-center distances extracted from the masks is reported in the insets of Figure 1A−C. They quantitatively confirm that the NPs are preferentially aligned along the

LiF nanoridges: across the ridges, the spacing is mainly dictated by the ridge periodicity Λ. Along the ridges, the strong next-neighbor NP spacing correlation is a consequence of the dynamics of the dewetting procedure. The NP spatial correlation is extremely high for *z*1 and gradually fades away with increasing coverage. In *z*3, some NPs indeed "spill" over the LiF ridges, coalescing with NPs in adjacent grooves and affecting the regularity of the array. The periodicities of the NP arrays along and across the LiF ridges (d_{001}, $d_{1\bar{1}0}$) deduced from these distributions are reported in Table 1. The array periodicity, consistently below 30 nm, implies a strong EM coupling between the NPs.

The metal/oxide fractions within the NPs were assessed by HR-XPS analysis. In Figure 2A, we report photoemission spectra of the Al 2p energy region for the *z*1 (top), *z*2 (middle), and *z*3 (bottom) areas acquired at room temperature within a few hours from the sample preparation. The X-ray beam was incident along the [100] direction, and the emitted electrons were analyzed along the [010] direction (see Figure 2B).

The spectra consist of two well-resolved peaks, due to metallic and oxidized atoms, at lower and higher binding energies, respectively.[42] The peaks have been fitted, after Berg *et al.*,[42] as a superposition of Doniach-Šunjič doublets with a fixed spin−orbit splitting of 0.42 eV and 1/2 branching ratio. The peak width was left free to vary between the metallic and the oxide component, and a Shirley-type background was employed. The metallic component (red area) increased in relative weight for increasing NP volume, while the oxide peak (green area) stayed roughly constant. The ratio *R* between the areas of the oxide and the metal peaks is *R* = 3.6, 2.7, and 2.2 for *z*1, *z*2, and *z*3, respectively. *R* is a very sensitive function of the NP metal and oxide relative fractions that change as the NP volume varies. For a fixed volume, *R* also depends on the NP shape, due to the limited XPS probing depth, so that the oxide/metal fraction in the NPs is not simply proportional to the respective areas of the XPS peaks. The NP shape therefore had to be deduced by appropriately modeling the XPS peak intensity. To this end, we had to make some basic assumptions about the NP shape and composition: we modeled the NPs as core−shell half-ellipsoids (Figure 2B) laid on the (010) LiF facets, neglecting the NP size dispersion. We assumed that the metal core was covered on the atmosphere side by an oxide shell with thickness t_{ox} = 2 nm,[16] and the in-plane aspect ratio of the half-ellipsoids was assumed to be equal to unity for simplicity and because no evidence of NP elongation was obtained by AFM data.

The in-plane radius of the metal core was defined as x_{met} and the out-of-plane metal core height z_{met}. When N_{Al} and t_{ox} are set, z_{met} becomes a function of x_{met} *only*. Thus, the ratio *R*, which clearly depends on the NP shape, also becomes a function of the metallic-core radius x_{met} only. The $R(x_{met})$ functional dependence was thus calculated for each experimental value of N_{Al} (*z*1, *z*2, and *z*3) in the geometry depited in Figure 2B. We assumed that the ionization cross sections of the metallic and the oxide species were proportional to the respective Al atom densities, and we fixed the electron mean free path in the two species

TABLE 1. Geometric Parameters[a]

zone	N_{Al}	d_{001} (nm)	$d_{1\bar{1}0}$ (nm)	x_{met} (nm)	z_{met} (nm)
*z*1	6×10^4	(21.5 ± 4)	(25.4 ± 4)	6.3 ± 2.6	5.7 ± 2.2
*z*2	1.2×10^5	(25.4 ± 6)	(25.4 ± 5)	9.1 ± 3.9	6.4 ± 2.8
*z*3	2.2×10^5	(29.3 ± 9)	(29.3 ± 6)	12.3 ± 5.1	7.4 ± 3.1

[a] Average number of Al atoms per NP, next-neighbor spacing along and across the LiF ridges (d_{001}, $d_{1\bar{1}0}$), mean radius (x_{met}), and out-of-plane height (z_{met}) of the Al metal NP core for the three zones.

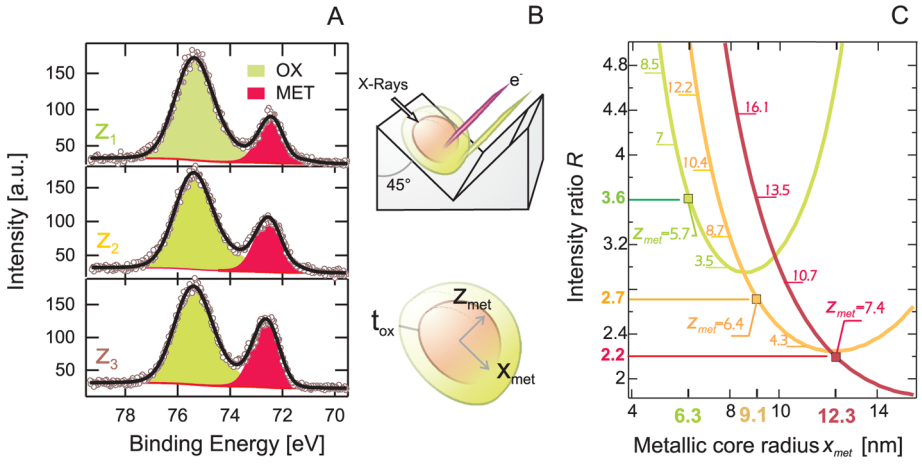

Figure 2. (A) Experimental high-resolution XPS spectra of the Al 2p region for *z*1 (top), *z*2 (middle), and *z*3 (bottom) (markers). The solid black line is a fit to the experimental data. The green (red) areas represent the contribution of Al atoms in oxidized (metallic) state. (B) Geometry for the XPS measurements (top) and for the XPS intensity calculations (bottom). (C) Calculated dependence of the oxide/metal XPS peak intensity ratio *R* as a function of the NP metallic-core radius x_{met}: *z*1 (green line), *z*2 (orange line), and *z*3 (red line). The experimental *R* values are reported as the green, orange, and red markers, respectively.

at l_{met} = 2.2 nm and l_{ox} = 2.4 nm[43] and assumed no attenuation of the X-rays through the Al NPs. In Figure 2C, we report the $R(x_{met})$ curves calculated for *z*1 (green line), *z*2 (orange line), and *z*3 (red line).

The broad size dispersion of the NPs implies that the smaller (larger) particles exhibit a larger (smaller) relative oxide content. However, introducing the finite size dispersion does not affect, to the first order, the calculated ratio *R* since small particles showing larger *R* will be counterbalanced by larger ones, yielding smaller *R*. The oxide thickness t_{ox} = 2 nm represents the expected value for Al within 24 h from exposure to atmosphere.[16] Changing this value within a reasonable range (1.8 nm < t_{ox} < 2.2 nm) merely introduces an additional uncertainty in x_{met}, on the order of ±15%, to be incoherently added to the AFM-deduced experimental size dispersion. The possibility of a size-dependent t_{ox}, though realistic, cannot be experimentally verified and was thus not included in the model.

The actual x_{met} and z_{met} corresponding to each zone could thus be deduced comparing the calculated *R* with the respective experimental values (Figure 2C), yielding the mean x_{met} and z_{met} values, reported in Table 1. For some N_{Al}, the model yields two solutions (*e.g.*, for *z*1); however, the highest x_{met} corresponds to an unphysically low z_{met}. The mean *total* (metal and oxide) in-plane NP diameters thus read $d = 17 \pm 5, 22 \pm 8$, and 29 ± 10 nm for *z*1, *z*2, and *z*3, respectively, nicely approaching the small-particle limit. We notice that, according to simple geometrical considerations, only the NPs of *z*1 can fit onto the (010) facet whose mean size is equal to $\Lambda/\sqrt{2} \approx 18$ nm. The NPs of *z*2 and *z*3 likely accommodate such "extra" volume by slightly elongating along the ridge direction or spilling onto the (100) facet.

Plasmonic Response. The optical response of the arrays was assessed by transmission measurements in the 2.75/12 eV photon energy range, performed at the BEAR beamline of the Elettra synchrotron radiation facility.[44−46] The transmission spectra were acquired at room temperature, at normal incidence, with linearly polarized light. The degree of linear polarization was 0.89 at 7.9 eV and 0.86 at 10.3 eV. The polarization direction was aligned either parallel or perpendicular to the LiF ridge direction. We will refer to these geometries as longitudinal (L) or transverse (T), respectively.

In Figure 3, the extinction spectra, normalized to the nanopatterned bare LiF, for *z*1 (panel A) and *z*3 (panel B) in longitudinal (open markers) and transverse (solid markers) geometries are shown. The spectra are characterized by strong peaks, easily ascribable to the LSPR excitation, in the 4−6 eV energy range. In T geometry, the LSPR is systematically higher in energy, reaching 5.8 eV in *z*1 and 5.55 eV in *z*3, with extinction of 0.18 and 0.48, respectively. In L geometry, the LSPRs are redshifted and broadened and exhibit an almost constant energy that evolves from 4.4 to 4.25 eV going from *z*1

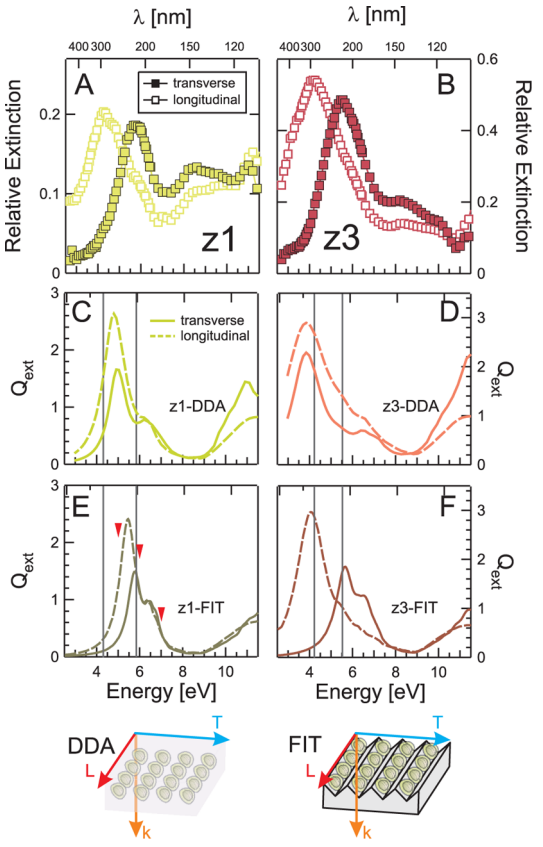

Figure 3. (A,B) Experimental extinction of the Al/LiF NP arrays, normalized to the bare LiF substrate, as a function of photon energy: *z*1 (A), *z*3 (B). Measurements in longitudinal (transverse) geometry are shown as open (solid) markers. (C−F) Calculated far-field extinction coefficients for *z*1 and *z*3 in longitudinal (dashed lines) and transverse (continuous lines) configurations using the parameters in Table 1. Calculations in panels C and D have been performed by means of DDA and calculations in panels E and F by FIT. The thin gray lines in panels C−F indicate the experimental peak positions. The red arrows in panel E correspond to the energies for which near-field maps are reported in Figure 4. Bottom: Geometries employed for DDA and FIT simulations.

to *z*3 and extinction of 0.20 and 0.54. In addition to these intense peaks, weaker features, whose relative weight with respect to the main peak increases for smaller NP size, are observed at energies slightly above 8 eV and appear to be more pronounced for T than L geometry. The NP size distribution is expected to add an inhomogeneous broadening to the LSP peaks. However, despite the significant size dispersion, the low-energy peaks are remarkably sharp, likely due to the spreading of the hybridized super-radiant LSP modes over several NPs that effectively limits the effects of disorder.[47] The optical spectra for *z*2 (not reported) exhibit LSPR energies and extinction that are intermediate between *z*1 and *z*3.

Calculations. The use of optical models to understand the optical properties of NPs and design them to better perform in the chosen application is becoming a fundamental tool in the development of

plasmonic materials for energy and sensing applications. When treating the optical response of an object, the exact analytical solution to Maxwell's equations only exists for perfect spheres and infinite cylinders and it is known as Mie theory.[1] For nonspherical particles, various numerical methods have been proposed in recent years. It is now widely accepted that size and shape have an important effect on the linear[4,48,49] and nonlinear[50−52] optical response of metallic NPs, especially in the case of noble metals such as Ag and Au. Only recently the attention has moved toward Al NPs,[18,20] but theoretical studies on systems based on real Al NPs are still fairly uncommon.

In Figure 3C,D (E,F), the calculated far-field extinction spectra for *z*1 and *z*3 are presented as obtained from DDA (FIT) calculations. The methods employed and the systems' geometries adopted are described in the Materials and Methods section.

In Figure 3C−F, the vertical lines represent the position of the experimental L and T peaks. Similar to what is observed experimentally (Figure 3A,B), several peaks can be observed in the calculated spectra. All the spectra are characterized by a lower-energy dominant peak, accompanied by a more or less pronounced shoulder on its high-energy side at ∼6−6.5 eV and by a further feature at higher energies (≳11 eV) more accentuated for the T than the L spectra. Both DDA and FIT succeed in reproducing fairly well the L spectra shape, while more significant discrepancies appear when comparing the experimental and calculated T-polarized spectra, especially in the high-energy range.

In *z*1, none of the simulation schemes succeeds in correctly reproducing the large (1.4 eV) LSP birefringence. DDA yields a 0.2 eV separation between L and T peaks, while FIT yields a slightly larger value of 0.4 eV. The calculated peaks for *z*1 have higher energy for FIT than for DDA. For *z*1, however, we found that slightly compressing the NPs along z_{met} or slightly elongating them along the [001] direction returns larger L−T splitting, suggesting that the uncertainty in the NP shape has some influence on the mismatch between experimental and calculated birefringence (see DDA calculations as a function of the in-plane NP aspect ratio in the Supporting Information). In *z*3, instead, FIT calculations yield almost perfectly matched L and T peak positions, correctly reproducing both the experimental LSPR energy and the L−T birefringence. In *z*3, with the NP diameter being larger than the (010) facet, the NP was artificially cut at the intersection of the (010) and (100) planes. DDA, while yielding spectral shapes more nicely matching the experiment, is not successful in reproducing the correct peak energy and the birefringence, indicating that, in this case, a correct handling of the substrate[53] with its peculiar asymmetry is best suited for reproducing the corresponding LSP asymmetry.

In order to delve deeper into the physical effects underlying the plasmonic response, we performed

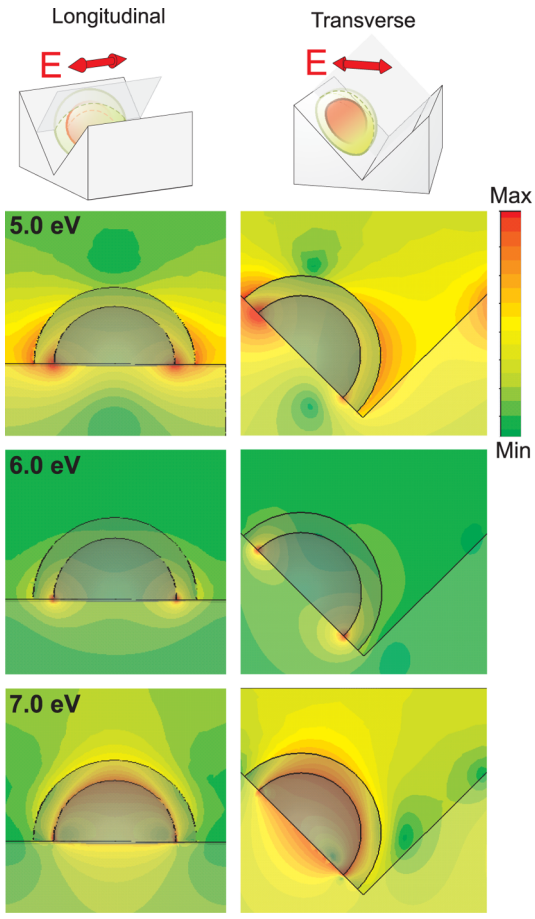

Figure 4. Top: Schematic representation of the optical geometry employed for the near-field-map calculations. The near-field maps represent the electric-field amplitude on the planes bisecting the NP as shown in the figures. Left column: Scalar amplitude near-field maps calculated in longitudinal configuration at energies of 5.0, 6.0, and 7.0 eV. Right column: Scalar amplitude near-field maps calculated in transverse configuration at energies of 5.0, 6.0, and 7.0 eV.

calculations of the local electric-field distribution in the NP arrays, at selected photon energies, by FIT. In Figure 4, we report electric-field amplitude maps calculated for *z*1 in L (left column) and T (right column) configurations at energies of 5.0, 6.0, and 7.0 eV, that is, at energies below the main peak, between the main peak and the high-energy shoulder and above the high-energy shoulder. At the lower investigated energy, the electric-field distribution has an underlying dipolar symmetry, as expected, whereas higher-order modes are clearly present at higher energy, more clearly discernible in the T geometry. The NP hybridization at the low-energy peak is present in both L and T geometries and clearly stronger in the L case, due to the smaller interparticle gap along the ridge direction. The stronger hybridization along the LiF ridges accounts for the broadening and red shifting of the *L* peaks with respect to their T counterparts. The high-energy structures in the spectra can be assigned to the onset of higher-order-like multipole modes in the Al NPs.

Since the spectrum of NPs, and Al in particular, is known to be extremely sensitive to changes in geometrical parameters,[20,25,54] the nonperfect matching of the calculated data with the experimental ones, in Figure 3, can be ascribed to the necessary simplification of the system in the optical models. It is interesting to notice that the calculations match generally well the experimental lowest-frequency dipolar mode, while discrepancies appear when considering higher-energy features. The good matching of the dipolar mode is likely due to its super-radiant dipolar character, resulting from the hybridization of adjacent NPs,[55−58] whose energy only weakly depends on morphological size/position disorder.[47] On the contrary, higher-order modes that are typically more sensitive to morphological disorder and to particle/shape effects are more complex to reproduce when addressing nonideal systems like ours.[47] The discrepancies between calculations and experiments are more apparent for T excitation. We speculate that this is due to the greater sensitivity of plasmon modes in this geometry to variations of the NP shape, arising from the lower system's symmetry along the [1$\bar{1}$0] direction.

Another interesting effect induced by the interparticle interaction is an increase in the contribution of scattering to the extinction spectra. All the NP sizes considered in this work are small enough that the extinction spectra of the single NPs is largely dominated by absorption; however, when the interparticle distance becomes comparable with the particle size, as in *z*2 and *z*3, it is possible to observe a crossover in the weight of the two contributions (absorption *vs* scattering) for the peak associated with the particle LSPR along the *x* major axis (see the Supporting Information).

CONCLUSIONS

In conclusion, we have fabricated arrays of aluminum NPs with a size approaching the small-particle (Rayleigh) limit that exhibit sharp LSPR response at extremely high energies (low wavelengths) in the deep ultraviolet region of the EM spectrum. The NPs were fabricated by means of a straightforward purely self-organization scheme as 2D arrays with extensions up to the cm^2, densities $>10^{11}$ NP/cm^{-2}, and interparticle gaps consistently below 10 nm. Their plasmonic response was modeled by DDA and FIT, achieving good agreement with the experimental data. Despite the small NP size, a strong plasmonic response could be observed even after exposure to atmosphere and subsequent oxidation. The ease of fabrication, the excellent performances, and the stability of the Al NP arrays represent a step toward broader application of deep ultraviolet plasmonics, such as ultraviolet Raman spectroscopy, sensing, and photovoltaics.

MATERIALS AND METHODS

Sample Preparation. The samples were fabricated following the procedure sketched in the top part of Figure 1. Optical-quality, flat LiF(110) crystals (10 × 10 × 1 mm^3, Crystec Gmbh) were first inserted in a vacuum chamber (base pressure p_{base} = 1.5 × 10^{-8} mbar) and flashed at 700 K in vacuum to remove physisorbed molecules. Approximately, 240 nm LiF was then homoepitaxially deposited from a heated crucible at a substrate temperature of 590 K, leading to the spontaneous formation of a regular nanometric uniaxial ridge-valley pattern at the LiF(110) surface, consisting of evenly spaced [100] and [010] exposed facets separated by nanoridges,[6,59,60] with a periodicity $\Lambda \approx 25$ nm. The LiF crystals used in this experiment were transparent up to an energy $E > 11.5$ eV, hence perfectly suited for DUV transmission experiments. Al films with equivalent thickness (defined as the thickness of the deposited material assuming a uniform substrate coverage) between 1.7 and 3.4 nm were deposited at grazing incidence (60° from the normal) on the nanopatterned LiF(110) by molecular beam epitaxy at a pressure $p < 2.5 \times 10^{-8}$ mbar. The system was flashed at $T = 670$ K in vacuum for 5 min to promote the dewetting of Al and then exposed to a flux of research-grade oxygen ($p = 1 \times 10^{-5}$ mbar × 200 s) at a temperature $T \approx 350$ K before being taken to atmosphere. The samples were characterized by AFM, XPS, and DUV optical spectroscopy within 24 h of their preparation. XPS was performed on a cleaved sample fragment, which was not later used for optical characterization due to the X-ray-induced formation of color centers in the substrate.

The Al thickness was calibrated by *ex situ* spectroscopic ellipsometry (SE) on a reference Al film (∼20 nm thick) grown on a LiF(001) single crystal (see the Supporting Information). The thick Al films exhibit the typical bulk-like optical response. For fitting their optical response, tabulated bulk Al optical constants were used.[33] Since SE allows one to distinguish metallic and oxide phases, it is possible to calibrate the sample thickness in terms of *number* of deposited Al atoms per unit area employing the known Al atomic densities in the two phases, C_{metal} = 100.14 × 10^{-24} mol/nm^3 and C_{ox} = 71.85 × 10^{-24} mol/nm^3.[43]

AFM images were acquired by means of a Multimode/Nanoscope IV system, Digital Instruments-Veeco, in tapping mode. XPS spectra were acquired by means of PHI ESCA 5600 system, monochromatized Al source. A neutralizer electron gun was used to compensate for charging effects.

DDA Method. DDA is a numerical method that was first proposed by Purcell and Pennypacker in 1973 for interstellar dielectric grains[61] and has been amply reviewed and developed by Draine and co-workers.[62−64] Draine and Flatau implemented DDA in an open-source Fortran 90 program, DDSCAT, that has been recently extended to include 2D periodic structures[65] (latest version of the program is 7.2[66]). Briefly, in DDA, the continuous particle is replaced with a cubic lattice of *N* point dipoles. The total field to which each dipole is exposed is the sum of the external electric field and the fields emitted by the other dipoles.[62] The interdipole distance has been chosen to be as small as possible while keeping a reasonable computing time for the periodic structure: 0.2 nm for *z*1, 0.25 nm for *z*2, and 0.3 nm for *z*3, corresponding ∼140 000 dipoles for each NP.

As discussed in refs 62, 64, and 66, the problem of electromagnetic scattering of an incident wave by an array of *N* point dipoles can be cast in the form **AP** = **E**, where **E** is the 3*N*-dimensional (complex) vector of the electric field at the *N* lattice sites, **P** is a 3*N*-dimensional (complex) vector of the (unknown) dipole polarizations, and **A** is a 3*N* × 3*N* complex matrix. Since 3*N* is a large number, iterative methods for solving this system of equations for the unknown vector **P** are preferred to direct methods. In this work, PBCGS2 was chosen as the algorithm for solving the system of equations while the polarizability has been prescribed using the GKDLDR option.[66]

FIT Method. FIT is a powerful numerical method for solving electromagnetic problems. It is especially capable of solving

large and detailed structures. It was first introduced by Thomas Weiland in 1977.[67] It is based on the solution of the Maxwell equations in their integral form. This approach allows the division of the overall simulation domain in smaller portions (units) with each of them being separately solved. Continuity relations among adjacent units provide the consistency of the general electromagnetic solution. Naturally, the kind of mesh chosen for FIT simulations can be crucial to obtaining correct results. In the present case, we have adopted a tetrahedral mesh, which is especially suitable for curved surfaces. The FIT method allows the calculation in both near- and far-field; hence quantities such as electric-field distributions or exctinction spectra can be efficiently determined by this numerical technique. Finally, in the present study, the convergence analysis approach has been especially stressed, due to the strongly irregular morphology of the structure. In this way, the error drops below 5% on the near-field calculations and less than 1% for the far-field results.

Optical Modeling. In all DDA calculations, the NPs are considered as immersed in a matrix where the patterned LiF substrate and vacuum medium have been replaced by a Bruggeman effective medium approximation (BEMA).[68] The dielectric function of this matrix, ε_M, can be obtained using the equation:

$$f_A\frac{\varepsilon_A - \varepsilon_M}{\varepsilon_A + 2\varepsilon_M} + f_B\frac{\varepsilon_B - \varepsilon_M}{\varepsilon_B + 2\varepsilon_M} = 0$$

where A and B refer to the constituent materials, in our case, LiF and vacuum, and *f* indicates the volume fraction, in the present case 50%.

Contrary to the DDA method, in the FIT calculations, it is possible to define a substrate (nanopatterned LiF), surrounding medium (air), and metallic nanoparticles with an oxide shell as three well-defined entities in the simulations, making the effective medium approximation unnecessary.

The optical constants for Al are from ref 33, while those for Al_2O_3 and LiF from ref 69 and are shown in the Supporting Information.

Conflict of Interest: The authors declare no competing financial interest.

Acknowledgment. G.G. thanks Daniel De Marco for help with setting up the DDSCAT 7.2 software package and with the Fortran code, and Stefan Kooij for helpful discussions on DDA. We thank Duc Chinh Vu for assistance in the sample preparation. Financial support from the Fondazione Carige, the University of Genova (PRA 2012), and the MIUR (Project No. PRIN 2008AKZSXY_002) is acknowledged. The computational work at Temple was supported in part by the Air Force Office for Scientific Research through research Grant No. FA9550-13-1-0094 and by the National Science Foundation through major research instrumentation Grant No. CNS-09-58854.

Supporting Information Available: Spectroscopic ellipsometry data and fit for the Al film deposited on LiF, as well as the optical constants used in DDA calculations and additional DDA extinction spectra as described in the text. This material is available free of charge *via* the Internet at http://pubs.acs.org.

REFERENCES AND NOTES

1. Bohren, C.; Huffman, D. *Absorption and Scattering of Light by Small Particles*; Wiley: New York, 1998.
2. Kreibig, U.; Genzel, L. Optical Absorption of Small Metal Particles. *Surf. Sci.* **1985**, *156*, 678–700.
3. El-Sayed, M. A. Some Interesting Properties of Metals Confined in Time and Nanometer Space of Different Shapes. *Acc. Chem. Res.* **2001**, *34*, 257–264.
4. Kelly, K. L.; Coronado, E.; Zhao, L. L.; Schatz, G. C. The Optical Properties of Metal Nanoparticles: The Influence of Size, Shape, and Dielectric Environment. *J. Phys. Chem. B* **2003**, *107*, 668–677.
5. Noguez, C. Surface Plasmons on Metal Nanoparticles: The Influence of Shape and Physical Environment. *J. Phys. Chem. C* **2007**, *111*, 3806–3819.
6. Anghinolfi, L.; Moroni, R.; Mattera, L.; Canepa, M.; Bisio, F. Flexible Tuning of Shape and Arrangement of Au Nanoparticles in 2-Dimensional Self-Organized Arrays: Morphology and Plasmonic Response. *J. Phys. Chem. C* **2011**, *115*, 14036–14043.
7. Henglein, A.; Gutierrez, M.; Janata, E.; Ershov, B. G. Absorption Spectrum and Chemical Reactions of Colloidal Cadmium in Aqueous Solution. *J. Phys. Chem.* **1992**, *96*, 4598–4602.
8. Henglein, A.; Giersig, M. Radiolytic Formation of Colloidal Tin and Tin-Gold Particles in Aqueous Solution. *J. Phys. Chem.* **1994**, *98*, 6931–6935.
9. Zorić, I.; Zäch, M.; Kasemo, B.; Langhammer, C. Gold, Platinum, and Aluminum Nanodisk Plasmons: Material Independence, Subradiance, and Damping Mechanisms. *ACS Nano* **2011**, *5*, 2535–2546.
10. Bonanni, V.; Bonetti, S.; Pakizeh, T.; Pirzadeh, Z.; Chen, J.; Nogués, J.; Vavassori, P.; Hillenbrand, R.; Akerman, J.; Dmitriev, A. Designer Magnetoplasmonics with Nickel Nanoferromagnets. *Nano Lett.* **2011**, *11*, 5333–5338.
11. Ekinci, Y.; Solak, H. H.; Löffler, J. F. Plasmon Resonances of Aluminum Nanoparticles and Nanorods. *J. Appl. Phys.* **2008**, *104*, 083107.
12. Blaber, M. G.; Arnold, M. D.; Ford, M. J. Search for the Ideal Plasmonic Nanoshell: The Effects of Surface Scattering and Alternatives to Gold and Silver. *J. Phys. Chem. C* **2009**, *113*, 3041–3045.
13. Langhammer, C.; Yuan, Z.; Zorić, I.; Kasemo, B. Plasmonic Properties of Supported Pt and Pd Nanostructures. *Nano Lett.* **2006**, *6*, 833–838.
14. Chen, J.; Wiley, B.; McLellan, J.; Xiong, Y.; Li, Z.-Y.; Xia, Y. Optical Properties of Pd-Ag and Pt-Ag Nanoboxes Synthesized *via* Galvanic Replacement Reactions. *Nano Lett.* **2005**, *5*, 2058–2062.
15. Xiong, Y.; Chen, J.; Wiley, B.; Xia, Y.; Yin, Y.; Li, Z.-Y. Size-Dependence of Surface Plasmon Resonance and Oxidation for Pd Nanocubes Synthesized *via* a Seed Etching Process. *Nano Lett.* **2005**, *5*, 1237–1242.
16. Langhammer, C.; Schwind, M.; Kasemo, B.; Zorić, I. Localized Surface Plasmon Resonances in Aluminum Nanodisks. *Nano Lett.* **2008**, *8*, 1461–1471.
17. Castro-Lopez, M.; Brinks, D.; Sapienza, R.; van Hulst, N. F. Aluminum for Nonlinear Plasmonics: Resonance-Driven Polarized Luminescence of Al, Ag, and Au Nanoantennas. *Nano Lett.* **2011**, *11*, 4674–4678.
18. Chan, G. H.; Zhao, J.; Schatz, G. C.; Duyne, R. P. V. Localized Surface Plasmon Resonance Spectroscopy of Triangular Aluminum Nanoparticles. *J. Phys. Chem. C* **2008**, *112*, 13958–13963.
19. Zeman, E. J.; Schatz, G. C. An Accurate Electromagnetic Theory Study of Surface Enhancement Factors for Silver, Gold, Copper, Lithium, Sodium, Aluminum, Gallium, Indium, Zinc, and Cadmium. *J. Phys. Chem.* **1987**, *91*, 634–643.
20. Hu, J.; Chen, L.; Lian, Z.; Cao, M.; Li, H.; Sun, W.; Tong, N.; Zeng, H. Deep-Ultraviolet-Blue-Light Surface Plasmon Resonance of Al and Al_{core}/Al_2O_{3shell} in Spherical and Cylindrical Nanostructures. *J. Phys. Chem. C* **2012**, *116*, 15584–15590.
21. Hornyak, G. L.; Phani, K. L. N.; Kunkel, D. L.; Menon, V. P.; Martin, C. R. Fabrication, Characterization and Optical Theory of Aluminum Nanometal/Nanoporous Membrane Thin Film Composites. *Nanostruct. Mater.* **1995**, *6*, 839–842.
22. Jiao, X.; Blair, S. Polarization Multiplexed Optical Bullseye Antennas. *Plasmonics* **2012**, *7*, 39–46.
23. Jeyaram, Y.; Jha, S. K.; Agio, M.; Löffler, J. F.; Ekinci, Y. Magnetic Metamaterials in the Blue Range Using Aluminum Nanostructures. *Opt. Lett.* **2010**, *35*, 1656–1658.
24. Taguchi, A.; Saito, Y.; Watanabe, K.; Yijian, S.; Kawata, S. Tailoring Plasmon Resonances in the Deep-Ultraviolet by Size-Tunable Fabrication of Aluminum Nanostructures. *Appl. Phys. Lett.* **2012**, *101*, 081110.
25. Knight, M. W.; Liu, L.; Wang, Y.; Brown, L.; Mukherjee, S.; King, N. S.; Everitt, H. O.; Nordlander, P.; Halas, N. J. Aluminum Plasmonic Nanoantennas. *Nano Lett.* **2012**, *12*, 6000–6004.

26. Ferry, V. E.; Polman, A.; Atwater, H. A. Modeling Light Trapping in Nanostructured Solar Cells. *ACS Nano* **2011**, *5*, 10055–10064.
27. Kochergin, V.; Neely, L.; Jao, C.-Y.; Robinson, H. D. Aluminum Plasmonic Nanostructures for Improved Absorption in Organic Photovoltaic Devices. *Appl. Phys. Lett.* **2011**, *98*, 133305.
28. Akimov, Y.; Koh, W. Design of Plasmonic Nanoparticles for Efficient Subwavelength Light Trapping in Thin-Film Solar Cells. *Plasmonics* **2011**, *6*, 155–161.
29. Jha, S. K.; Ahmed, Z.; Agio, M.; Ekinci, Y.; Löffler, J. F. Deep-UV Surface-Enhanced Resonance Raman Scattering of Adenine on Aluminum Nanoparticle Arrays. *J. Am. Chem. Soc.* **2012**, *134*, 1966–1969.
30. Thyagarajan, K.; Rivier, S.; Lovera, A.; Martin, O. J. Enhanced Second-Harmonic Generation from Double Resonant Plasmonic Antennae. *Opt. Express* **2012**, *20*, 12860–12865.
31. Taguchi, A.; Hayazawa, N.; Furusawa, K.; Ishitobi, H.; Kawata, S. Deep-UV Tip-Enhanced Raman Scattering. *J. Raman Spectrosc.* **2009**, *40*, 1324–1330.
32. Ehrenreich, H.; Philipp, H. R.; Segall, B. Optical Properties of Aluminum. *Phys. Rev.* **1963**, *132*, 1918–1928.
33. Shiles, E.; Sasaki, T.; Inokuti, M.; Smith, D. Y. Self-Consistency and Sum-Rule Tests in the Kramers-Kronig Analysis of Optical Data: Applications to Aluminum. *Phys. Rev. B* **1980**, *22*, 1612–1628.
34. Batson, P. E. Surface Plasmon Coupling in Clusters of Small Spheres. *Phys. Rev. Lett.* **1982**, *49*, 936–940.
35. Stöckli, T.; Bonard, J.-M.; Stadelmann, P.-A.; Châtelain, A. EELS Investigation of Plasmon Excitations in Aluminum Nanospheres and Carbon Nanotubes. *Z. Phys. D* **1997**, *40*, 425–428.
36. Lu, G.; Li, W.; Zhang, T.; Yue, S.; Liu, J.; Hou, L.; Li, Z.; Gong, Q. Plasmonic-Enhanced Molecular Fluorescence within Isolated Bowtie Nano-Apertures. *ACS Nano* **2012**, *6*, 1438–1448.
37. Mahdavi, F.; Blair, S. Nanoaperture Fluorescence Enhancement in the Ultraviolet. *Plasmonics* **2010**, *5*, 169–174.
38. Anno, E.; Tanimoto, M. Size-Dependent Change in Parallel Band Absorption of Al Particles. *Phys. Rev. B* **2001**, *64*, 165407.
39. Meziani, M. J.; Bunker, C. E.; Lu, F.; Li, H.; Wang, W.; Guliants, E. A.; Quinn, R. A.; Sun, Y.-P. Formation and Properties of Stabilized Aluminum Nanoparticles. *ACS Appl. Mater. Interfaces* **2009**, *1*, 703–709.
40. Stratakis, E.; Barberoglou, M.; Fotakis, C.; Viau, G.; Garcia, C.; Shafeev, G. A. Generation of Al Nanoparticles *via* Ablation of Bulk Al in Liquids with Short Laser Pulses. *Opt. Express* **2009**, *17*, 12650–12659.
41. Cabrera, N.; Mott, N. F. Theory of the Oxidation of Metals. *Rep. Prog. Phys.* **1948**, *12*, 163–184.
42. Berg, C.; Raaen, S.; Borg, A.; Andersen, J. N.; Lundgren, E.; Nyholm, R. Observation of a Low-Binding-Energy Peak in the 2p Core-Level Photoemission from Oxidized Al(111). *Phys. Rev. B* **1993**, *47*, 13063–13066.
43. Jeurgens, L.; Sloof, W.; Borsboom, C.; Tichelaar, F.; Mittemeijer, E. Determination of Total Primary Zero Loss Intensities in Measured Electron Emission Spectra of Bare and Oxidised Metals: Application to Aluminium Oxide Films on Aluminium Substrates. *Appl. Surf. Sci.* **2000**, *161*, 139–148.
44. Naletto, G.; Pelizzo, M. G.; Tondello, G.; Nannarone, S.; Giglia, A. Monochromator for the Synchrotron Radiation Beamline X-MOSS at ELETTRA. *Proc. SPIE* **2001**, *4145*, 105–113.
45. Nannarone, S.; Giglia, A.; Mahne, N.; DeLuisa, A.; Doyle, B.; Borgatti, F.; Pedio, M.; Pasquali, L.; Naletto, G.; Pelizzo, M. G.; *et al.* BEAR: A Bending Magnet for Emission, Absorption and Reflectivity. *Neutroni e Luce di Sincrotrone* **2007**, *12*, 8–19.
46. Nannarone, S.; Borgatti, F.; DeLuisa, A.; Doyle, B. P.; Gazzadi, G. C.; Giglia, A.; Finetti, P.; Mahne, N.; Pasquali, L.; Pedio, M.; *et al.* The BEAR Beamline at Elettra. *AIP Conf. Proc.* **2004**, *705*, 450–453.
47. Slaughter, L. S.; Willingham, B. A.; Chang, W.-S.; Chester, M. H.; Ogden, N.; Link, S. Toward Plasmonic Polymers. *Nano Lett.* **2012**, *12*, 3967–3972.
48. Kooij, E. S.; Poelsema, B. Shape and Size Effects in the Optical Properties of Metallic Nanorods. *Phys. Chem. Chem. Phys.* **2006**, *8*, 3349–3357.
49. Kooij, E. S.; Ahmed, W.; Zandvliet, H. J. W.; Poelsema, B. Localized Plasmons in Noble Metal Nanospheroids. *J. Phys. Chem. C* **2011**, *115*, 10321–10332.
50. Gonella, G.; Dai, H.-L. Determination of Adsorption Geometry on Spherical Particles from Nonlinear Mie Theory Analysis of Surface Second Harmonic Generation. *Phys. Rev. B* **2011**, *84*, 121402.
51. Gonella, G.; Gan, W.; Xu, B.; Dai, H.-L. The Effect of Composition, Morphology, and Susceptibility on Nonlinear Light Scattering from Metallic and Dielectric Nanoparticles. *J. Phys. Chem. Lett.* **2012**, *3*, 2877–2881.
52. Roke, S.; Gonella, G. Nonlinear Light Scattering and Spectroscopy of Particles and Droplets in Liquids. *Annu. Rev. Phys. Chem.* **2012**, *63*, 353–378.
53. Knight, M. W.; Wu, Y.; Lassiter, J. B.; Nordlander, P.; Halas, N. J. Substrates Matter: Influence of an Adjacent Dielectric on an Individual Plasmonic Nanoparticle. *Nano Lett.* **2009**, *9*, 2188–2192.
54. Albella, P.; Garcia-Cueto, B.; González, F.; Moreno, F.; Wu, P. C.; Kim, T.-H.; Brown, A.; Yang, Y.; Everitt, H. O.; Videen, G. Shape Matters: Plasmonic Nanoparticle Shape Enhances Interaction with Dielectric Substrate. *Nano Lett.* **2011**, *11*, 3531–3537.
55. Halas, N. J.; Lal, S.; Chang, W.-S.; Link, S.; Nordlander, P. Plasmons in Strongly Coupled Metallic Nanostructures. *Chem. Rev.* **2011**, *111*, 3913–3961.
56. Harris, N.; Arnold, M. D.; Blaber, M. G.; Ford, M. J. Plasmonic Resonances of Closely Coupled Gold Nanosphere Chains. *J. Phys. Chem. C* **2009**, *113*, 2784–2791.
57. Barrow, S. J.; Funston, A. M.; Gómez, D. E.; Davis, T. J.; Mulvaney, P. Surface Plasmon Resonances in Strongly Coupled Gold Nanosphere Chains from Monomer to Hexamer. *Nano Lett.* **2011**, *11*, 4180–4187.
58. Le, F.; Brandl, D. W.; Urzhumov, Y. A.; Wang, H.; Kundu, J.; Halas, N. J.; Aizpurua, J.; Nordlander, P. Metallic Nanoparticle Arrays: A Common Substrate for Both Surface-Enhanced Raman Scattering and Surface-Enhanced Infrared Absorption. *ACS Nano* **2008**, *2*, 707–718.
59. Sugawara, A.; Mae, K. Surface Morphology of Epitaxial LiF(110) and CaF_2(110) Layers. *J. Vac. Sci. Technol., B* **2005**, *23*, 443–448.
60. Kitahara, T.; Sugawara, A.; Sano, H.; Mizutani, G. Optical Second-Harmonic Spectroscopy of Au Nanowires. *J. Appl. Phys.* **2004**, *95*, 5002–5005.
61. Purcell, E. M.; Pennypacker, C. R. Scattering and Absorption of Light by Nonspherical Dielectric Grains. *Astrophys. J.* **1973**, *186*, 705–714.
62. Draine, B. T. The Discrete-Dipole Approximation and Its Application to Interstellar Graphite Grains. *Astrophys. J.* **1988**, *333*, 848–872.
63. Draine, B. T.; Goodman, J. Beyond Clausius-Mossotti—Wave-Propagation on a Polarizable Point Lattice and the Discrete Dipole Approximation. *Astrophys. J.* **1993**, *405*, 685–697.
64. Draine, B. T.; Flatau, P. J. Discrete-Dipole Approximation for Scattering Calculations. *J. Opt. Soc. Am. A* **1994**, *11*, 1491–1499.
65. Draine, B. T.; Flatau, P. J. Discrete-Dipole Approximation for Periodic Targets: Theory and Tests. *J. Opt. Soc. Am. A* **2008**, *25*, 2693–2703.
66. Draine, B. T.; Flatau, P. J. *User Guide for the Discrete Dipole Approximation Code DDSCAT 7.2*; http://arxiv.org/abs/1202.3424, 2012.
67. Weiland, T. A Discretization Method for the Solution of Maxwell's Equations for Six-Component Fields. *AEU Int. J. Electron. Commun.* **1977**, *31*, 116–120.
68. Bruggeman, D. A. G. Calculation of Various Physics Constants in Heterogenous Substances I Dielectricity Constants and Conductivity of Mixed Bodies from Isotropic Substances. *Ann. Phys.* **1935**, *24*, 636–679.
69. *Handbook of Optical Constants of Solids*; Palik, E. D., Ed.; Academic Press: New York, 1985; pp 369–406.